

Laser picoscopy of valence electrons in solids

<https://doi.org/10.1038/s41586-020-2429-z>

H. Lakhotia^{1,2,4}, H. Y. Kim^{1,2,4}, M. Zhan^{1,2}, S. Hu³, S. Meng³ & E. Goulielmakis^{1,2,✉}

Received: 29 April 2019

Accepted: 1 May 2020

Published online: 1 July 2020

 Check for updates

Valence electrons contribute a small fraction of the total electron density of materials, but they determine their essential chemical, electronic and optical properties. Strong laser fields can probe electrons in valence orbitals^{1–3} and their dynamics^{4–6} in the gas phase. Previous laser studies of solids have associated high-harmonic emission^{7–12} with the spatial arrangement of atoms in the crystal lattice^{13,14} and have used terahertz fields to probe interatomic potential forces¹⁵. Yet the direct, picometre-scale imaging of valence electrons in solids has remained challenging. Here we show that intense optical fields interacting with crystalline solids could enable the imaging of valence electrons at the picometre scale. An intense laser field with a strength that is comparable to the fields keeping the valence electrons bound in crystals can induce quasi-free electron motion. The harmonics of the laser field emerging from the nonlinear scattering of the valence electrons by the crystal potential contain the critical information that enables picometre-scale, real-space mapping of the valence electron structure. We used high harmonics to reconstruct images of the valence potential and electron density in crystalline magnesium fluoride and calcium fluoride with a spatial resolution of about 26 picometres. Picometre-scale imaging of valence electrons could enable direct probing of the chemical, electronic, optical and topological properties of materials.

The generation of high harmonics in solids^{7–12} has led to numerous advances in strong-field condensed-matter physics. High harmonics in solids are primarily interpreted as the result of the nonlinear driving of electrons within and between bands^{16–20}. High harmonics in solids are now used to probe the essential characteristics of solids, such as the band dispersion^{9,21,22}, the topology¹³, the dynamic conductivity²³ and the arrangement of atoms in the crystal lattice^{13,14}. Yet, the direct imaging of the valence electron potential and density of crystalline solids requires a description of light–matter interactions in solids within the framework of scattering^{24,25}, as typically used in atomic-scale diffraction microscopies²⁶.

It is now understood that laser fields can modify the electrostatic potential of solids and thereby be used to manipulate their electronic gaps and structure^{27–30}, providing ample opportunities for optical engineering of materials^{31,32}. Yet, the interpretation of the interaction of a laser and crystal electrons, and the associated nonlinear emission of radiation, within the framework of scattering is more demanding. The laser fields should be sufficiently strong and fast to effectively suppress the valence crystal potential so that it becomes a weak perturbation to the laser-driven motion of electrons. Ultrafast laser pulses³³, which are capable of damage-free exposure of bulk solids at fields that exceed their static dielectric strength by many orders of magnitude^{7–14,23,34}, could enable this possibility.

To better appreciate how a scattering regime could possibly emerge in the extreme nonlinear optics of solids, we consider the interaction of valence electrons in a crystal potential $V(r) = \sum_k V_k e^{ikr}$ with a laser field $F(t) = F_0 \sin(\omega_L t)$. Here k and V_k denote the reciprocal lattice vectors

and the Fourier components of the crystal potential, respectively, r is the spatial coordinate and i is the imaginary unit. F_0 and ω_L denote the amplitude and frequency of the laser field, respectively, and t is time. Following earlier studies of atoms and solids^{27–29,35–39} and by expressing the time-dependent Schrödinger equation within the reference frame of the moving electron under the laser field, the total potential experienced by a valence electron can be formulated as^{27–29}

$$U(r, t) = \sum_k V_k J_0 \left(\frac{kF_0}{\omega_L^2} \right) e^{ikr} + \sum_{N \neq 0, k} V_k J_N \left(\frac{kF_0}{\omega_L^2} \right) e^{i(kr - N\omega_L t)} \quad (1)$$

Here J_N is the Bessel function of the first kind and order N . The first sum of terms in equation (1) is time independent and describes an effective crystal potential $V_{\text{eff}}(r, F_0) = \sum_k V_k J_0 \left(\frac{kF_0}{\omega_L^2} \right) e^{ikr}$, the properties of which are modified by the laser field. This potential is analogous to the Krammer–Henneberger potential in atomic physics^{35–39}. The rest of the terms in equation (1) describe transitions (absorption and emission of photons at harmonic energies $N\omega$ of the fundamental field) among the states of the effective crystal potential^{36,37,39}. Thus, the character of the optical interaction can now be intuitively understood in the framework of the effective potential $V_{\text{eff}}(r, F_0)$ and its quantum states under the intense laser field F_0 .

The valence electrons can now be driven as quasi-free particles by an external laser^{27–29} when $V_{\text{eff}}(r, F_0) \approx 0$. For the dominant reciprocal-space vector of a crystal ($k = 2\pi/d$, where d is the lattice constant), this implies that $J_0 \left(\frac{kF_0}{\omega_L^2} \right) \approx 0$ and suggests that for a typical

¹Institut für Physik, Universität Rostock, Rostock, Germany. ²Max-Planck-Institut für Quantenoptik, Garching, Germany. ³Institute of Physics, Chinese Academy of Sciences, Beijing, China. ⁴These authors contributed equally: H. Lakhotia, H. Y. Kim. ✉e-mail: e.goulielmakis@uni-rostock.de

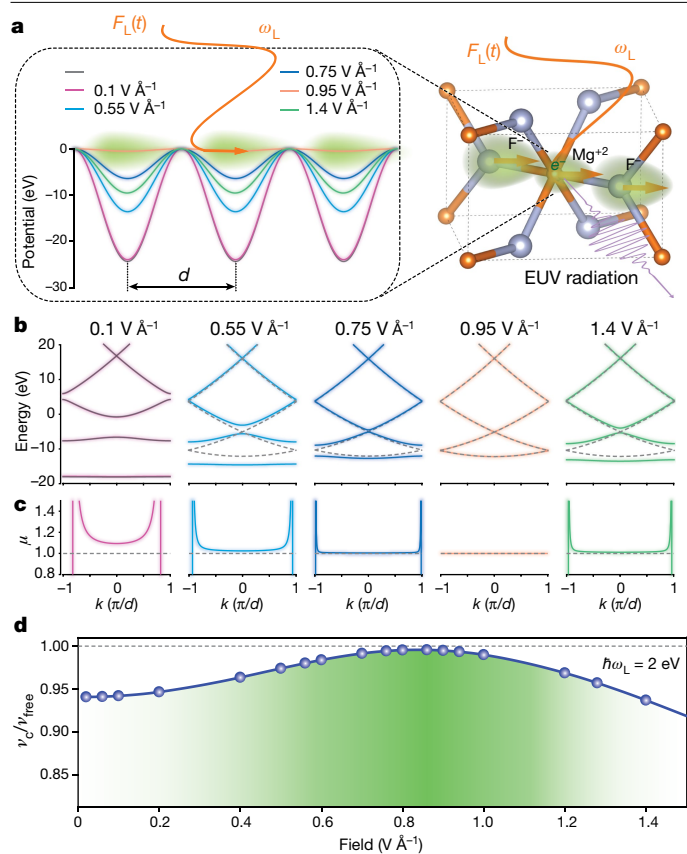


Fig. 1 | Strong-field quasi-free electron motion in a crystal. **a**, Effective crystal potential of MgF_2 along the [100] axis for intense optical ($\hbar\omega_L \approx 2 \text{ eV}$) fields of increasing strength ($0.1\text{--}1.4 \text{ V \AA}^{-1}$). The field-free crystal potential is shown as a black curve. Green shaded areas indicate the valence electron cloud. EUV, extreme ultraviolet. **b, c**, The band structure (**b**) and reduced effective mass (**c**) as calculated for the three lowest bands and for the corresponding field strengths shown in **a**. The black curve in **b** and **c** denotes the band structure and effective mass of the undressed solid, respectively. Dashed lines in **b** and **c** represent the band dispersion and effective mass of free electrons, respectively. **d**, Ratio of the maximum of crystal ($v_c(t)$) and free ($v_{\text{free}}(t)$) electron velocities along [100] direction of MgF_2 crystal calculated by TDDFT as a function of field strength of the driving pulse with a carrier photon energy of 2 eV. The blue curve and the grey dashed line are guides for the eye.

solid ($d = 2\text{--}7 \text{ \AA}$) exposed to an optical field ($\hbar\omega_L \approx 2 \text{ eV}$), a quasi-free electron motion will emerge for fields in the range of $0.4\text{--}1.4 \text{ V \AA}^{-1}$, typically attainable in strong-field experiments in solids^{9,11,23,34}.

Figure 1a (left) shows the modification of $V_{\text{eff}}(r, F_0)$ in magnesium fluoride (MgF_2 ; right) along the [100] direction as calculated by an optical field ($\hbar\omega_L \approx 2 \text{ eV}$) of gradually increasing F_0 . At low fields, $F_0 < 0.1 \text{ V \AA}^{-1}$, $V_{\text{eff}}(r, F_0)$ (Fig. 1a, magenta curve) is nearly identical to that of the unperturbed crystal (Fig. 1a, black curve). The associated band structure (Fig. 1b, magenta curve) and the reduced effective mass of carriers μ in the crystal (Fig. 1c, magenta curve) hardly differ from those of the undressed solid (black curve in Fig. 1b).

At higher fields, the effective potential $V_{\text{eff}}(r, F_0)$ is notably suppressed (Fig. 1a, cyan and blue curves). The band structure (Fig. 1b, cyan and blue curves) and μ (Fig. 1c, cyan and blue lines) are now gradually approaching that of the free electron (grey dashed lines in Fig. 1b, c, respectively). At the critical field strength $F_0 \approx 0.93 \text{ V \AA}^{-1}$ for which $J_0\left(\frac{kF_0}{\omega_L^2}\right) \approx 0$, the crystal potential is totally suppressed (Fig. 1a, orange curve). Bandgaps (Fig. 1b, orange curve) are now coherently closing^{27–29}, while the band dispersion (Fig. 1b, orange curve) and μ (Fig. 1c, orange curve) of the carriers in the crystal virtually match those of the free

electron (grey dashed curves in Fig. 1b, c, respectively). For ever higher fields, the $V_{\text{eff}}(r, F_0)$ revives (Fig. 1a, green curve), obeying the oscillatory nature of $J_0\left(\frac{kF_0}{\omega_L^2}\right)$, versus field F_0 (Fig. 1a). The reduced effective mass μ remains near that of the free electron (Fig. 1c, green line) for the best part of the Brillouin zone, but its sharp discontinuity at the edges is restored.

Figure 1 a–c clearly shows that the notion of quasi-free electron motion becomes plausible over a broad range of laser fields provided that the charge carriers in the crystal do not reach the edges of the Brillouin zone to experience a Bragg reflection. This implies that for the crystal momentum $k(t) < \pi/d$ and for the optical field amplitude $F_0 < \frac{\pi\omega_L}{d}$.

First-principle, time-dependent density functional theory (TDDFT) simulations in three dimensions (Fig. 1d) on crystalline MgF_2 exposed to few-cycle pulses ($\hbar\omega_L \approx 2 \text{ eV}$) with an electric field vector aligned with the [100] axis of the crystal support the above perspective (Methods). To allow an intuitive relation to Fig. 1 a–c, we calculated the velocity of the carriers in the bulk crystal $v_c(t)$ (see also Extended Data Fig. 1) and compared it with that of the free electrons $v_{\text{free}}(t)$, exposed to identical waveforms and for a wide range of optical field strengths. As the reduced effective mass μ in the crystal is approximately related to the velocity ratio as $v_c(t)/v_{\text{free}}(t) \approx 1/\mu$, this calculation allows us to place the perspective of Fig. 1 a–c under further scrutiny.

The ratio $v_c(t)/v_{\text{free}}(t)$, as evaluated at the maximum of $v_{\text{free}}(t)$, is shown in Fig. 1d. For weak fields, this ratio reflects the inverse of the reduced effective mass of carriers $1/\mu \approx 0.94$ around the Γ point of MgF_2 . For higher field strengths, the velocity of the crystal electrons rapidly increases and reaches that of the free electron at the critical field $F_0 \approx 0.95 \text{ V \AA}^{-1}$ (Fig. 1c, orange curve). For a further increase of the optical field $F_0 > \pi\omega_L/d$ (Fig. 1d), the simulations verify that electrons will experience Bragg reflection as manifested by the rapid drop in the carrier velocity in the crystal with respect to that of the free electrons.

Within the range of optical fields for which the crystal potential is considerably suppressed (Fig. 1a) and the band structure assumes a quasi-parabolic profile, the dynamics of the electronic wavefunction and concomitant emission of high harmonics may be treated within the framework of scattering and the motion of the electron in the potential can be described both classically²⁴ and quantum mechanically²⁵. For MgF_2 , this is further verified by comparing high-harmonic emission as described in these models with the results of the TDDFT simulations (Extended Data Fig. 2).

Within the scattering picture, the electric currents and emitted radiation are linked (Methods) to the valence periodic potential of the crystal as:

$$\frac{\partial \mathbf{J}}{\partial t} \propto N_e \sum_{\mathbf{k}} \mathbf{k} V_{\mathbf{k}} \sum_N J_N \left(\frac{\mathbf{k} \cdot \mathbf{F}_0}{\omega_L^2} \right) e^{iN\omega_L t} \quad (2)$$

where N_e is the number of electrons.

Extending to three dimensions (Methods), the intensity of the harmonics that are collinearly polarized with the unit vector of the laser polarization (\mathbf{e}_l) is linked with the periodic potential of the crystal as:

$$I_N(F_0, \omega_L, \mathbf{e}_l) \propto \left| N_e \sum_{k_1} \tilde{V}_{k_1} k_1 J_N \left(k_1 \frac{F_0}{\omega_L^2} \right) \right|^2 \quad (3)$$

where k_1 and \tilde{V}_{k_1} are the projections of the reciprocal space vectors and the Fourier components of the potential, respectively, onto the laser polarization vector. In the coordinate space (Fig. 1a), this operation represents a one-dimensional (1D) slice of the potential of the crystal $V_c(\mathbf{r})$, parallel to \mathbf{e}_l , passing through the expectation value of the position \mathbf{r}_0 of the initial electronic wavefunction within a unit cell. For crystals with a centre(s) of symmetry (C), \mathbf{r}_0 coincides with this centre(s). Equation (3) also implies that by measuring a set of N harmonics for

various laser strengths F_0 , the Fourier components \tilde{V}_{k_i} of a 1D slice (Fig. 1a, inset) of the crystal potential can be retrieved. As the intensity of every radiated harmonic of the field I_N (equation (3)) is associated with a broad range of \tilde{V}_{k_i} , the relative phase information—in contrast to linear techniques⁴⁰—among \tilde{V}_{k_i} is not lost; it is rather embodied in the recorded intensities I_N and thus can be also retrieved.

The highest radiated photon energy E_c (cut-off) and harmonic order N_c can now be estimated using the fact that the Bessel function in equation (3) reaches a maximum when its argument equals its order, N_c :

$$E_c = N_c \omega_L \approx \frac{k_{\max} F_0}{\omega_L} \quad (4)$$

Here, k_{\max} is the highest significant (cut-off) reciprocal vector of the crystal potential $V_c(\mathbf{r})$. As previously suggested²⁴, equation (4) represents a clear analogy between the high-harmonic emission and the Smith–Purcell effect⁴¹, where the radiation energy is the product of velocity and spatial frequency. k_{\max} is naturally associated with the valence radius r^h of the smallest atom/ion in the system, as $k_{\max} \approx 2\pi/r^h$.

Therefore, the cut-off law can also be expressed as $E_c \approx \frac{2\pi F_0}{r^h \omega_L}$, suggesting that within the scattering approximation, the dimensions of the smallest atomic or ionic radii in a crystal are directly linked to the cut-off energy and thus can be probed by measuring the cut-off energy as:

$$r^h \approx \frac{2\pi F_0}{E_c \omega_L} \quad (5)$$

Probing the ion/atomic radii in solids

In a first set of experiments, we interrogate the validity of the scattering picture by examining the possibility of probing the smallest ionic/covalent radii of atoms in solids with a sole measurement of the high-harmonic cut-off energy, as suggested by equation (5). In the experiments summarized in Fig. 2a, strong ($F_0 = 0.4\text{--}0.7\text{ V \AA}^{-1}$), few-cycle pulses (duration of about 5.5 fs) carried in the visible ($\hbar\omega_L \approx 2\text{ eV}$) generated harmonics in MgF_2 and other crystalline solids (Methods). The properties of the driving pulses—including the peak electric field F_0 and centroid carrier frequency ω_L —in these experiments are accessed by attosecond streaking⁴². Representative harmonic spectra recorded in MgF_2 when the laser polarization vector is aligned with the [110] and [100] crystal axes are shown in Fig. 2b. For MgF_2 , we record the cut-off energy E_c as a function of the optical field strength F_0 (Fig. 2c, black dots). We evaluate the corresponding slope of E_c versus the field strength F_0 in Fig. 2c (blue line) and derive the radius (equation (5)) as $r^h = 59 \pm 4\text{ pm}$. This result reasonably agrees with the empirical radius⁴³ of Mg^{+2} in MgF_2 (about 72 pm) and lies far from the corresponding radius of the much larger F^- (about 130 pm). To interrogate the character of these findings more generally, we extended the measurements to several crystalline materials, as summarized in Fig. 2d. The radii evaluated from these measurements (Fig. 2d, blue bars) once again agree well with the empirical predictions (Fig. 2d, red bars) and suggest that the scattering model is applicable in these systems.

Mapping of the crystal potential and electron density in MgF_2 and CaF_2

In a next set of experiments, we set the laser polarization parallel to a specific crystal direction by rotating the crystal (Fig. 2a) and recorded the harmonic yield I_N versus F_0 and the crystal angle (Extended Data Fig. 3). For the [110] and [100] crystal axes of MgF_2 , the recorded harmonic yields are shown in Fig. 3a, b, respectively. An excellent fit (Methods) of the experimental data (red and blue curves in Fig. 3a, b, respectively) using equation (3) is obtained for all harmonics. The retrieved amplitudes and phases of \tilde{V}_{k_i} are shown in Fig. 3c, d, respectively.

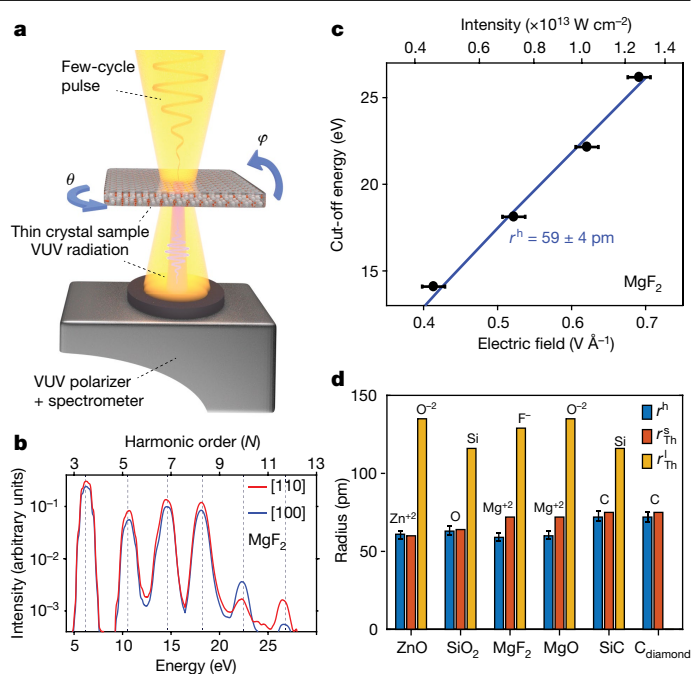


Fig. 2 | Probing of the ionic/covalent radius of atoms in solids.

a, Experimental setup for laser picoscopy. θ and φ denote the azimuthal angle and polar angle, respectively. **b**, Harmonic spectra generated in MgF_2 when the laser polarization vector is aligned with the [110] (red curve) and [100] (blue curve) axes of the crystal. **c**, High harmonic cut-off energy E_c (black dots) versus driving electric field amplitude F_0 for the [110] axis of the crystal. The ionic radius ($r^h = 59 \pm 4\text{ pm}$) of Mg^{+2} is evaluated by the slope of the data (blue line) according to equation (5). **d**, Measured (blue bars) and empirical (red bars) ionic/covalent radii of the smallest ions/atoms (r_{Th}^s) in ZnO , SiO_2 , MgF_2 , MgO , SiC and diamond crystals. The empirical valence radii of the largest ions/atoms (r_{Th}^l) in each crystal (orange bars) are shown for comparison. Error bars indicate the standard deviation of the mean value from three measurements acquired under identical conditions.

The inverse Fourier transform of these data yields the reconstructed, real-space potential shown in Fig. 4a, b. A measurement (Methods) along the [110] axis provides a 1D slice of the crystal potential along a line defined by the crystal symmetry point and the laser polarization vector \mathbf{e}_1 . In MgF_2 , this implies probing of the crystal potential along F–Mg–F axis on plane (002) (Fig. 3a). Indeed, the retrieved potential slice (Fig. 4a) is composed of three consecutive valleys, which can intuitively be assigned to the F^- , Mg^{+2} and F^- ion potentials, respectively. Yet, because a second symmetry point (C_2) of MgF_2 is located on plane (001), an additional 1D potential slice (along a line defined by C_2 and the laser polarization vector \mathbf{e}_1) contributes to the measurement. The addition of these two 1D potential slices practically results in the duplication of the Mg^{+2} contribution on the measured potential curve of Fig. 4a. Along the [100] axis (Fig. 4b), the potential consists of a single valley that can be primarily assigned to an Mg^{+2} ion on plane (001) plus that from an Mg^{+2} ion on plane (002). A weak contribution from the spatially extended F^- ions is also anticipated (Fig. 4b, top) and results in the broadening of the Mg^{+2} peak (Fig. 4b, blue curve).

On the basis of the data in Fig. 4a, b, as well as additional data retrieved for the intermediate crystal direction [120], we reconstruct the full ‘on plane’ potential of MgF_2 , as shown in Fig. 4c (Methods). We also evaluate the corresponding valence electron density $n(r)$ on the basis of the Thomas–Fermi approximation as $n(r) \propto V(r)^{3/2}$, shown in Fig. 4d. The potential and electron density data in Fig. 4c, d indicate that the Mg–F ‘molecular pattern’ exhibits a four-fold rotational symmetry, compatible with the notion of ‘simultaneous’ probing of crystal planes carrying symmetry points. This aspect is further supported by the

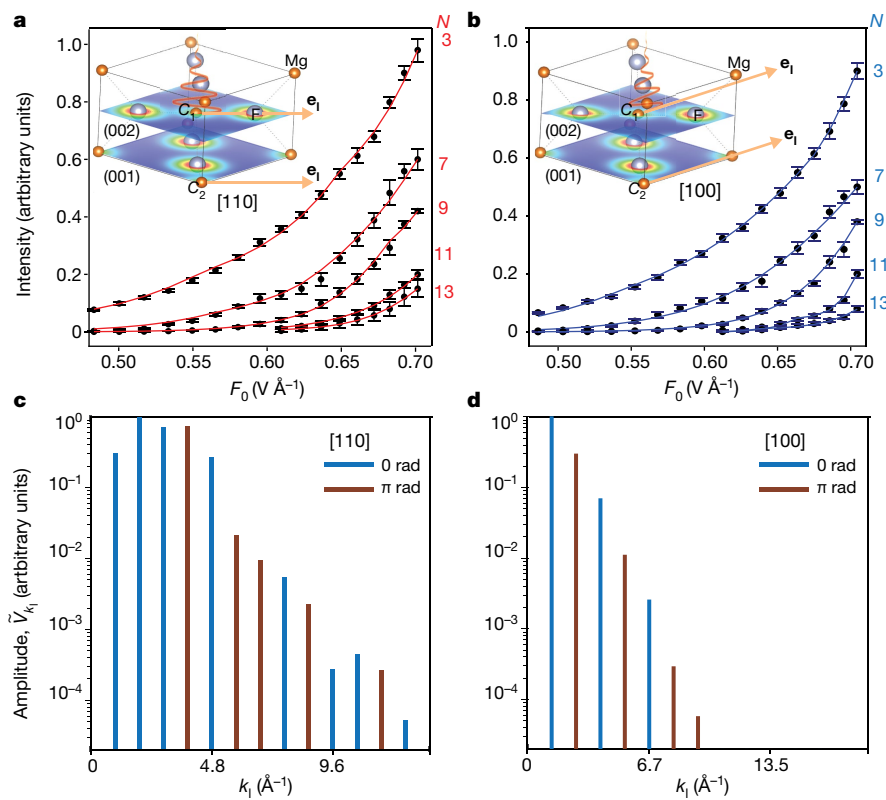


Fig. 3 | Measurement of the Fourier coefficients of the crystal potential in MgF₂. **a, b**, Intensity yields (black dots) of the emitted harmonics versus driving field strength F_0 as measured along the [110] (**a**) and [100] (**b**) axes of the crystal and their fittings according to equation (3), in red curves and blue curves, respectively. Error bars indicate the standard deviation of the mean value of four measurements acquired under identical conditions. Insets: MgF₂ crystal structure and DFT-calculated electron density for planes (001) and (002). The symmetry points C_1 and C_2 of the crystal are shown on the corresponding planes. The laser polarization vector (orange arrow) and the symmetry points C_1 and C_2 determine the lines along which the Fourier coefficients of potential are probed. **c, d**, Retrieved amplitudes \tilde{V}_{k_i} and relative phases (0 rad in blue and π rad in red) along the [110] (**c**) and [100] (**d**) axes of the crystal, respectively.

simulations of Fig. 4e, which show the electron density resulting from the addition of the densities of planes (001) and (002) laterally shifted so that the symmetry points (Mg^{+2}) in each plane coincide.

The reconstructed images of the valence electrons in Fig. 4c, d enable the visualization of the atomic-scale, electronic properties of MgF₂. The electron radius of Mg^{+2} can now be directly deduced from the electron density curve (Fig. 4f)—as $r_{\text{Mg}^{+2}}^h \approx 76$ pm, which

matches the empirical radius of Mg^{+2} (about 72 pm) with better accuracy compared with the estimative measurements based on the cut-off method (Fig. 2c). We also evaluate the corresponding radius of F^- as $r_{\text{F}^-}^h \approx 126$ pm, which is also in agreement with the empirical data (about 130 pm).

The direct measurement of the valence electron structure in solids with picometre accuracy in these systems enables a direct comparison

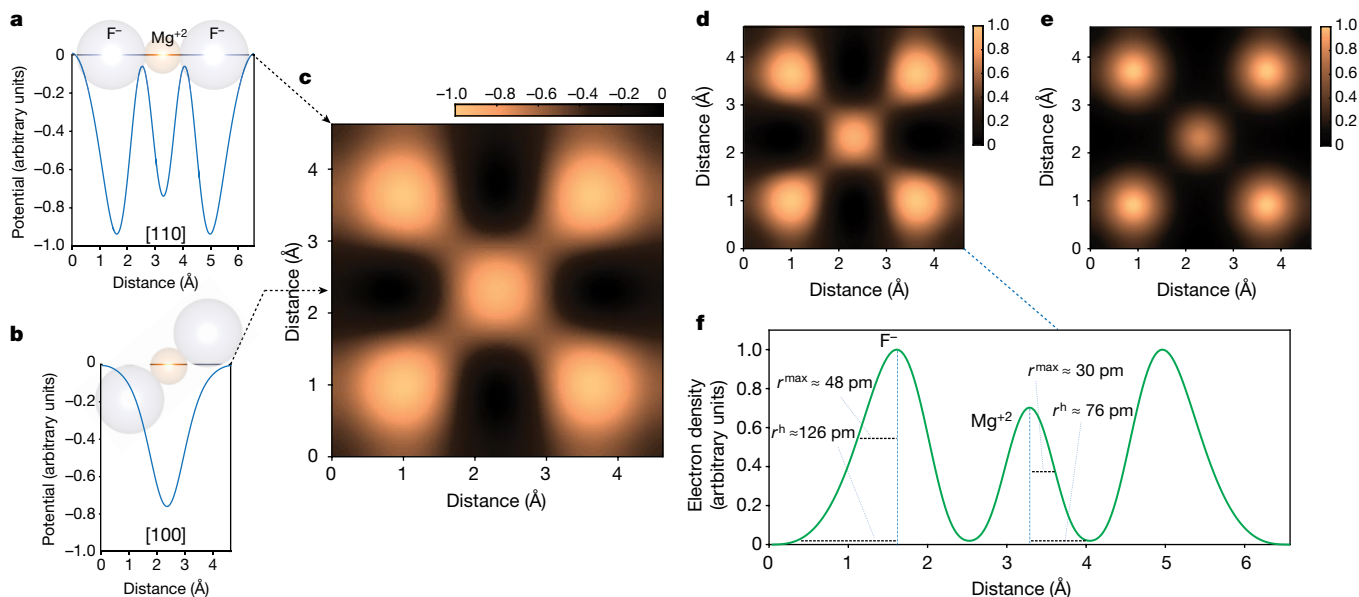


Fig. 4 | Reconstruction of the valence electron potential and density of MgF₂. **a, b**, Reconstructed 1D slices of the valence potential (blue curves) when the laser polarization vector is aligned with the [110] (**a**) and [100] (**b**) axes. Grey and orange spheres represent F^- and Mg^{+2} ions, respectively, as aligned along the probed line of the crystal. **c**, A reconstructed 2D slice of the valence electron potential of MgF₂. The Mg^{+2} ion is in the centre, surrounded by F^- ions. **d**, Valence electron density derived from the data in **c**. **e**, DFT-simulated

electron density of MgF₂ summed over the (001) and (002) planes and shifted such that the symmetry points (C_1 and C_2 as shown in the insets of Fig. 3a, b) on both the planes coincide. **f**, Electron density (green curve) along the F–Mg–F axis of the MgF₂ crystal derived from the experimentally reconstructed valence electron potential shown in **a**. Black dashed lines indicate the evaluated ionic radii (r^h) and (r^{max}) as defined in the text.

of experimental and rigorously calculated quantum mechanical quantities. The electron radius, which is often associated with essential properties of materials such as the polarizability and diamagnetic susceptibility, is defined as the principal maximum (r^{\max}) of the radial density distribution function⁴⁴. Evaluations of r^{\max} from the retrieved data for each ion in Fig. 4f yielded $r_{\text{Mg}^{2+}}^{\max} \approx 30$ pm and $r_{\text{F}^-}^{\max} \approx 48$ pm. Once again, these values closely match the theoretically calculated radii of 27 pm and 44 pm for Mg^{2+} and F^- , respectively⁴⁴. We further benchmarked the capability of laser picoscopy to image the valence electronic structure by extending our experimental study to a system with a rather different crystalline structure: calcium fluoride (CaF_2 , fluorite) (Methods, Extended Data Figs. 4–6).

An inspection of the reconstructed potential and/or electron density distributions in the two studied systems provides information on the nature of chemical bonding. In particular, the considerable differences in the evaluated radii of the crystal ions compared with those of neutral atoms (Mg, 167 pm; F, 41 pm; Ca, 275 pm)⁴⁵ is compatible with the electron transfer from Mg and Ca to F, (Fig. 4d, Extended Data Fig. 5e, respectively) occurring during the chemical bond formation. Moreover, in MgF_2 , the weak potential (Fig. 4c) and electron density (Fig. 4d) in the interstitial space between anions and cations is compatible with the ionic character of the underlying chemical bond.

The spatial resolution attained with laser picoscopy may be directly inferred from the highest reciprocal space vectors k_{\max} , which are substantial in the fitting of the corresponding intensity yields in Fig. 3c, d. For example, measurements along the [100] axis of MgF_2 yielded $k_{\max} = 12.2 \text{ \AA}^{-1}$, suggesting a spatial resolution of about 26 pm, that is, approximately half of the Bohr radius in atomic hydrogen.

Direct imaging of valence electrons in bulk solids with picometre resolution may broaden the scope of modern, atomic-scale microscopy to include direct access to the chemical, electronic and topological properties of matter. Future experiments, including these in other spectral ranges of the driving field and detailed examination and extension of the theoretical premises of picoscopy, will be required to verify the applicability of the technique to a broader range of materials. Laser picoscopy is readily incorporable with time-resolved spectroscopies and could enable the tracking of simultaneously unfolding atomic and valence electron dynamics with picometre and attosecond resolution. It may also enable a route to the detailed understanding of the phase transition dynamics of matter.

Online content

Any methods, additional references, Nature Research reporting summaries, source data, extended data, supplementary information, acknowledgements, peer review information; details of author contributions and competing interests; and statements of data and code availability are available at <https://doi.org/10.1038/s41586-020-2429-z>.

- Itatani, J. et al. Tomographic imaging of molecular orbitals. *Nature* **432**, 867–871 (2004).
- Haessler, S. et al. Attosecond imaging of molecular electronic wavepackets. *Nat. Phys.* **6**, 200–206 (2010).
- Villeneuve, D. M., Hockett, P., Vrakking, M. J. J. & Niikura, H. Coherent imaging of an attosecond electron wave packet. *Science* **356**, 1150–1153 (2017).
- Smirnova, O. et al. High harmonic interferometry of multi-electron dynamics in molecules. *Nature* **460**, 972–977 (2009).
- Baker, S. et al. Probing proton dynamics in molecules on an attosecond time scale. *Science* **312**, 424–427 (2006).
- Kübel, M. et al. Spatiotemporal imaging of valence electron motion. *Nat. Commun.* **10**, 1042 (2019).
- Ghimire, S. et al. Observation of high-order harmonic generation in a bulk crystal. *Nat. Phys.* **7**, 138–141 (2011).
- Schubert, O. et al. Sub-cycle control of terahertz high-harmonic generation by dynamical Bloch oscillations. *Nat. Photon.* **8**, 119–123 (2014).
- Luu, T. T. et al. Extreme ultraviolet high-harmonic spectroscopy of solids. *Nature* **521**, 498–502 (2015).
- Vampa, G. et al. Linking high harmonics from gases and solids. *Nature* **522**, 462–464 (2015); corrigendum **542**, 260 (2017).
- Ndabashimiye, G. et al. Solid-state harmonics beyond the atomic limit. *Nature* **534**, 520–523 (2016).
- Sivis, M. et al. Tailored semiconductors for high-harmonic optoelectronics. *Science* **357**, 303–306 (2017).
- You, Y. S., Reis, D. A. & Ghimire, S. Anisotropic high-harmonic generation in bulk crystals. *Nat. Phys.* **1**, 1–6 (2016).
- You, Y. S., Cunningham, E., Reis, D. A. & Ghimire, S. Probing periodic potential of crystals via strong-field re-scattering. *J. Phys. At. Mol. Opt. Phys.* **51**, 114002 (2018).
- von Hoegen, A., Mankowsky, R., Fechner, M., Först, M. & Cavalleri, A. Probing the interatomic potential of solids with strong-field nonlinear phononics. *Nature* **555**, 79–82 (2018).
- Golde, D., Meier, T. & Koch, S. W. High harmonics generated in semiconductor nanostructures by the coupled dynamics of optical inter- and intraband excitations. *Phys. Rev. B* **77**, 075330 (2008).
- Vampa, G., McDonald, C. R., Orlando, G., Corkum, P. B. & Brabec, T. Semiclassical analysis of high harmonic generation in bulk crystals. *Phys. Rev. B* **91**, 064302 (2015).
- Wu, M., Ghimire, S., Reis, D. A., Schafer, K. J. & Gaarde, M. B. High-harmonic generation from Bloch electrons in solids. *Phys. Rev. A* **91**, 043839 (2015).
- Higuchi, T., Stockman, M. I. & Hommelhoff, P. Strong-field perspective on high-harmonic radiation from bulk solids. *Phys. Rev. Lett.* **113**, 213901 (2014).
- Kemper, A. F., Moritz, B., Freericks, J. K. & Devereaux, T. P. Theoretical description of high-order harmonic generation in solids. *New J. Phys.* **15**, 023003 (2013).
- Vampa, G. et al. All-optical reconstruction of crystal band structure. *Phys. Rev. Lett.* **115**, 193603 (2015).
- Lanin, A. A., Stepanov, E. A., Fedotov, A. B. & Zheltikov, A. M. Mapping the electron band structure by intraband high-harmonic generation in solids. *Optica* **4**, 516–519 (2017).
- Garg, M. et al. Multi-petahertz electronic metrology. *Nature* **538**, 359–363 (2016).
- Hüller, S. & Meyer-Ter-Vehn, J. High-order harmonic radiation from solid layers irradiated by subpicosecond laser pulses. *Phys. Rev. A* **48**, 3906–3909 (1993).
- Kálmán, P. & Brabec, T. Generation of coherent hard-X-ray radiation in crystalline solids by high-intensity femtosecond laser pulses. *Phys. Rev. A* **52**, R21–R24 (1995).
- Warren, B. E. *X-ray Diffraction* (Courier Corporation, 1990).
- Tzoar, N. & Gersten, J. Theory of electronic band structure in intense laser fields. *Phys. Rev. B* **12**, 1132–1139 (1975).
- Miranda, L. C. M. Energy-gap distortion in solids under intense laser fields. *Solid State Commun.* **45**, 783–785 (1983).
- Holthaus, M. The quantum theory of an ideal superlattice responding to far-infrared laser radiation. *Z. Phys. B* **89**, 251–259 (1992).
- Gruzdev, V. E. Photoionization rate in wide band-gap crystals. *Phys. Rev. B* **75**, 205106 (2007).
- Wang, Y. H., Steinberg, H., Jarillo-Herrero, P. & Gedik, N. Observation of Floquet-Bloch states on the surface of a topological insulator. *Science* **342**, 453–457 (2013).
- McIver, J. W. et al. Light-induced anomalous Hall effect in graphene. *Nat. Phys.* **16**, 38–41 (2020).
- Brabec, T. & Krausz, F. Intense few-cycle laser fields: frontiers of nonlinear optics. *Rev. Mod. Phys.* **72**, 545–591 (2000).
- Schultze, M. et al. Controlling dielectrics with the electric field of light. *Nature* **493**, 75–78 (2013).
- Henneberger, W. C. Perturbation method for atoms in intense light beams. *Phys. Rev. Lett.* **21**, 838–841 (1968).
- Gavrila, M. & Kamiński, J. Z. Free-free transitions in intense high-frequency laser fields. *Phys. Rev. Lett.* **52**, 613–616 (1984).
- Gavrila, M. Atomic stabilization in superintense laser fields. *J. Phys. At. Mol. Opt. Phys.* **35**, R147–R193 (2002).
- Morales, F., Richter, M., Patchkovskii, S. & Smirnova, O. Imaging the Kramers–Henneberger atom. *Proc. Natl Acad. Sci. USA* **108**, 16906–16911 (2011).
- Medišauskas, L., Saalmann, U. & Rost, J.-M. Floquet Hamiltonian approach for dynamics in short and intense laser pulses. *J. Phys. At. Mol. Opt. Phys.* **52**, 015602 (2019).
- Taylor, G. The phase problem. *Acta Crystallogr. D* **59**, 1881–1890 (2003).
- Smith, S. J. & Purcell, E. M. Visible light from localized surface charges moving across a grating. *Phys. Rev.* **92**, 1069 (1953).
- Goutlielmakis, E. et al. Direct measurement of light waves. *Science* **305**, 1267–1269 (2004).
- Shannon, R. D. Revised effective ionic radii and systematic studies of interatomic distances in halides and chalcogenides. *Acta Crystallogr. A* **32**, 751–767 (1976).
- Ghosh, D. C. & Biswas, R. Theoretical calculation of absolute radii of atoms and ions. Part 2. The ionic radii. *Int. J. Mol. Sci.* **4**, 379–407 (2003).
- Ghosh, D. C. & Biswas, R. Theoretical calculation of absolute radii of atoms and ions. Part 1. The atomic radii. *Int. J. Mol. Sci.* **3**, 87–113 (2002).

Publisher's note Springer Nature remains neutral with regard to jurisdictional claims in published maps and institutional affiliations.

© The Author(s), under exclusive licence to Springer Nature Limited 2020

Methods

DFT and TDDFT simulations in MgF₂

The time-dependent simulations were performed using the time-dependent ab initio package (TDAP)^{46,47} within the framework of DFT and TDDFT⁴⁸. First, the laser–matter interaction was included in the Hamiltonian to simulate the effect of external laser field: $\hat{H} = \frac{1}{2m}(\hbar\mathbf{k} - \frac{e}{c}\hat{A}, \hat{A}, t)^2 + \hat{V}_c$, where m , e and k are the electron mass, charge and momentum, respectively, V_c is the periodic potential of the crystal and $\hat{A}(t) = -c \int \hat{E}(t) dt$ (ref. 49) is the vector potential of the driving pulse. c is the speed of light. The time-dependent Kohn–Sham equation (TDKS) was propagated in real time, where the propagator operator is expressed within the Crank–Nicolson scheme^{46,50}. Then, the TDKS orbitals $\psi_{G,k,\sigma}(t)$ as well as the time-dependent charge density $\rho(r, t)$ were obtained at each timestep. The time-dependent electron velocity $v_{G,k,\sigma}(t)$ was calculated from the TDKS orbitals:

$$v_{G,k,\sigma}(t) = -i \sum_i \left[\psi_{i,G,k,\sigma}(t) |\nabla| \psi_{i,G,k,\sigma}(t) - \psi_{i,G,k,\sigma}(t) |\nabla| \psi_{i,G,k,\sigma}(t)^* \right] \quad (6)$$

where i labels the state index and G, k and σ are the planewave-basis, k point and spin index, respectively. We derive the total electron velocity as:

$$\mathbf{v}(t) = \frac{1}{V_{\text{cell}}} \sum_{G,k,\sigma} v_{G,k,\sigma}(t) \quad (7)$$

where V_{cell} is the volume of the unit cell. More details about the algorithm can be found in refs. 46,47. The velocity of the free electron was trivially obtained from the vector potential $A(t)$ as: $v(t)_{\text{free}} = \hbar A(t)/m$, where m is the free electron mass. In the calculations, we considered laser pulses with the characteristics of those used in the experiments. We used norm-conserving pseudopotentials with the Perdew–Burke–Ernzerhof functional⁵¹. To reduce the computation time, we opted for the numerical atomic orbitals as well as an auxiliary real-space grid equivalent to a planewave cut-off of 150 Rydberg. The k -points sampling was $6 \times 6 \times 9$. The evolution of the system was calculated by self-consistently propagating the electron density and the results are convergent with timesteps from 2 to 20 as.

To obtain the valence electron density and electrical potential, the SIESTA DFT package⁵² was used with the PBE⁵¹ functional and numerical atomic orbitals basis set. For sampling, $12 \times 12 \times 18$ points in 3D k -space were used, and a density matrix was calculated to obtain the electron density. The reduced effective mass in MgF₂ was estimated on the basis of two valence and two conduction bands within the same DFT code.

High-harmonic generation in the semi-classical limit

The emission of harmonics from a solid driven by an intense laser field $\mathbf{F}_L(t) = F_0 \sin(\omega_L t) \mathbf{e}_1$ is associated with rate of change of the induced current in its bulk. Under conditions for which the crystal potential is softened by the intense field and the corresponding band structure, in turn, becomes a quasi-parabolic profile as presented in the main text, the kinematics of the electrons can be treated semi-classically by introducing the limit⁵³ $\nabla V_c(\mathbf{r}(t)) \approx \nabla V_c(\langle \mathbf{r}(t) \rangle)$. In this limit, the current variation in time is governed by the classical equation of motion according to the Ehrenfest theorem.

$$\frac{\partial}{\partial t} \mathbf{J}(t) \approx -N_e \nabla V_c(\mathbf{r}(t)) \approx -N_e \nabla V_c(\langle \mathbf{r}(t) \rangle) \quad (8)$$

$V_c(\langle \mathbf{r}(t) \rangle)$ in this case represents the potential of N_e valence electrons in the crystal, and $\langle \mathbf{r}(t) \rangle$ stands for the classical expectation value of the position of the wavepacket within a unit cell of a crystal following the electric field of the laser as $\langle \mathbf{r}(t) \rangle = \left(\mathbf{r}_0 + \frac{F_0}{\omega_L^2} \sin(\omega_L t) \right) \cdot \mathbf{r}_0$ is the expectation value of the initial position of the electron wavefunction within a

unit cell. The periodic potential can now be expressed in terms of its Fourier coefficients $V_c(\mathbf{r}) = \sum_{\mathbf{k}} V_{\mathbf{k}} e^{-i(\mathbf{k} \cdot \mathbf{r})}$

$$\frac{\partial}{\partial t} \mathbf{J}(t) \approx -N_e \nabla \sum_{\mathbf{k}} V_{\mathbf{k}} e^{-i\mathbf{k} \cdot \langle \mathbf{r}(t) \rangle} = iN_e \sum_{\mathbf{k}} \mathbf{k} V_{\mathbf{k}} e^{-i\mathbf{k} \cdot \left(\mathbf{r}_0 + \frac{F_0}{\omega_L^2} \sin(\omega_L t) \right)} \quad (9)$$

The exponential term in the above equation can be further expanded using the Jacobi–Anger expansion. The real part of $\frac{\partial}{\partial t} \mathbf{J}(t)$ can be decomposed into odd and even terms such as:

$$\frac{\partial}{\partial t} \mathbf{J}(t) = \frac{\partial}{\partial t} \mathbf{J}^{\text{odd}}(t) + \frac{\partial}{\partial t} \mathbf{J}^{\text{even}}(t)$$

where

$$\frac{\partial}{\partial t} \mathbf{J}^{\text{odd}}(t) \approx N_e \sum_{\mathbf{k}} \mathbf{k} \text{Re}(V_{\mathbf{k}}) \sum_{n=1}^{\infty} J_{2n-1} \left(\frac{\mathbf{k} \cdot \mathbf{F}_0}{\omega_L^2} \right) \sin[(2n-1)\omega_L t] \quad (10)$$

$$\frac{\partial}{\partial t} \mathbf{J}^{\text{even}}(t) \approx N_e \sum_{\mathbf{k}} \mathbf{k} \text{Im}(V_{\mathbf{k}}) \sum_{n=1}^{\infty} J_{2n} \left(\frac{\mathbf{k} \cdot \mathbf{F}_0}{\omega_L^2} \right) \cos[(2n)\omega_L t] \quad (11)$$

where J_N is the Bessel function of the first kind and order N , and $\text{Re}(V_{\mathbf{k}})$ and $\text{Im}(V_{\mathbf{k}})$ are the real and the imaginary parts of $V_{\mathbf{k}}$. The intensity I_N of a radiated harmonic of order N as a function of the field strength F_0 and driving frequency ω_L is given by a square modulus of the Fourier transform of the rate of change of the total current. In the experiments presented here, only centrosymmetric crystals were used ($\text{Im}(V_{\mathbf{k}}) = 0$), hence only odd harmonics are relevant. The intensity I_N of the odd harmonics can be further decomposed into components parallel (\mathbf{e}_1) and perpendicular (\mathbf{e}_\perp) to the laser polarization vector:

$$I_N(F_0, \omega_L, \mathbf{e}_1) \propto \left| N_e \sum_{\mathbf{k}} \mathbf{k} \cdot \mathbf{e}_1 V_{\mathbf{k}} J_N \left(\frac{\mathbf{k} \cdot \mathbf{F}_0}{\omega_L^2} \right) \right|^2 \quad (12)$$

$$I_N(F_0, \omega_L, \mathbf{e}_\perp) \propto \left| N_e \sum_{\mathbf{k}} \mathbf{k} \cdot \mathbf{e}_\perp V_{\mathbf{k}} J_N \left(\frac{\mathbf{k} \cdot \mathbf{F}_0}{\omega_L^2} \right) \right|^2 \quad (13)$$

Notably, the results of equations (12) and (13) closely match those of previous studies that treated the problem classically²⁴ or quantum mechanically²⁵.

All the factors except $V_{\mathbf{k}}$ inside the summation in equation (12) depend on \mathbf{k} through $\mathbf{k} \cdot \mathbf{e}_1$. This fact is used to split the summation into two parts, one in the direction of laser polarization (\mathbf{e}_1) and other perpendicular to it (\mathbf{e}_\perp). The summation of the Fourier coefficients of the potential $V_{\mathbf{k}}$ in the perpendicular direction (\mathbf{e}_\perp) is given as:

$$\tilde{V}_{\mathbf{k}_\perp} = \sum_{\mathbf{k}_\perp} V_{\mathbf{k}_\perp + \mathbf{k}_1} \quad (14)$$

where $\mathbf{k} = \mathbf{k}_1 + \mathbf{k}_\perp$ such that $k_1 = \mathbf{k} \cdot \mathbf{e}_1$ and $k_\perp = \mathbf{k} \cdot \mathbf{e}_\perp$ are the projection of reciprocal space vector in the direction parallel and perpendicular to laser polarization, respectively. According to the Fourier slice theorem⁵⁴, the Fourier transform of $\tilde{V}_{\mathbf{k}_\perp}$ represents a 1D slice of the potential in the \mathbf{e}_1 direction, passing through the origin \mathbf{r}_0 . Hence, the emitted radiation $I_N(F_0, \omega_L, \mathbf{e}_1)$ is associated with the motion of the electron along this slice. In this case, equation (12) is reduced to a scalar form:

$$I_N(F_0, \omega_L, \mathbf{e}_1) \propto \left| N_e \sum_{k_1} \tilde{V}_{k_1} k_1 J_N \left(k_1 \frac{F_0}{\omega_L^2} \right) \right|^2 \quad (15)$$

An important implication of the scattering approximation as suggested by the derivations summarized in equation (15) or equation (3) is that, as the valence electron cloud, in the entire volume of the unit cell, can be considered free to move under the driving field, its dynamics can be described by the temporal evolution of the expectation value of the

wavefunction $\mathbf{r}(t)$ (single-point dynamics). The weak perturbation from the crystal potential to the electron-cloud motion induces coherent currents and consequentially harmonic radiation. Harmonic yields calculated by TDDFT and the scattering model are in a good agreement (Extended Data Fig. 2).

Experimental

MgF₂, MgO, CaF₂, SiO₂, ZnO and diamond crystals with thickness of about 2 μm or less were placed in a vacuum chamber and were exposed to few-cycle (about 5.5 fs) pulses carried at about 2 eV. The pulses were produced by a second-generation light-field synthesizer⁵⁵. The field strength F_0 of the laser pulses on the sample was varied by a precisely adjustable aperture. The detailed field waveform (including the amplitude F_0 and the carrier frequency ω_1) of the pulses was measured using attosecond streaking⁴². The vacuum ultraviolet (VUV) radiation emerging from the sample was polarization-filtered by reflection off two rhodium-coated concave mirrors placed at a quasi-grazing incidence (about 78°) as well as a flat-field VUV grating (about 75°). The intensity of the perpendicular polarized (\mathbf{e}_\perp) component of the emitted high harmonics was suppressed by a factor of about 20 compared with the parallel polarized component (\mathbf{e}_\parallel). The grating was also used to disperse the harmonic spectrum on a microchannel plate-phosphor screen detector. A high-dynamic-range charge-coupled device camera recorded images of high-harmonic spectra versus the driving field strength and the crystal angle. Cut-offs in all measurements were defined as the last harmonic energy detectable by our detection system. Owing to a strong contamination of the fifth harmonic signal by second-order diffractions of the grating, its intensity dependence has been omitted in the potential reconstruction of MgF₂.

Reconstructing 1D slices of the crystal potential

The intensity yields I_n of the recorded harmonics versus driving field amplitude F_0 were used to retrieve the amplitudes and phases of the Fourier coefficients of the 1D slice of the crystal potential as described by equation (15) or equation (3). As in this first study we are interested in the relative amplitudes and phases among these coefficients, the intensity yields of all harmonics were normalized to unity. This step is essential in the reconstruction process as it prevents artefacts that relate to the accurate knowledge of the relative yields of harmonics. The latter can be affected by the transmission of the specimen and the intensity calibration of the detection system—especially over the extended spectral ranges of study.

A least-squares fitting algorithm (Levenberg–Marquardt) was used to fit the experimental data within MATLAB R2016b. The fitting converged rapidly and yielded a regression better than 3%. The linear slices of the potential resulting from the inverse Fourier transform of the projected coefficients are plotted in arbitrary amplitude units.

Strictly, equation (15) or equation (3) are accurate for a monochromatic light field. In the case of a pulsed driving field, the equation of motion for the total current can be expressed as

$$\frac{\partial}{\partial t} \mathbf{J}(t) \propto iN_e \sum_{\mathbf{k}} \mathbf{k} V_{\mathbf{k}} e^{-i\mathbf{k} \cdot \left(\frac{\mathbf{F}_1(t)}{\omega_1^2} \right)} \quad (16)$$

where $\mathbf{F}_1(t)$ denotes the field waveform of the driving pulse. Harmonic spectra calculated directly by equation (16) are shown in Extended Data Fig. 2b. A complete reconstruction of the Fourier coefficients can also be achieved using the above formula with $\mathbf{F}_1(t)$ being the experimentally measured electric field waveform. Yet for electric field strengths up to about 1.2 V Å⁻¹, the analytical form remains accurate under an adjustment of the field amplitude F_{0N} used in the reconstruction of the intensities for each harmonic N as

$$F_{0N} = F_0 \frac{\sqrt{N\pi}}{2} \operatorname{erf} \left(\frac{1}{\sqrt{N}} \right) \quad (17)$$

where F_0 is the peak field strength of the driving pulse. In this case, the use of the quasi-analytic formulas in the main text allows a broader applicability of the technique proposed and implemented here and can also be applied in experimental facilities where a field-resolved characterization of light waveforms is not currently available.

Scattering picture and crystallography

For crystals with the rutile-structure MgF₂ in our study, the expectation value of the initial wavefunction coincides with the symmetry points of the crystal, which are the Mg⁺² ions (marked as C_1 and C_2) on planes (001) and (002) (Fig. 3a, b, insets). As a result, when the polarization vector of the laser is, for example aligned with the [100] axis of MgF₂, the 1D slice of the potential probed will be on a line defined by the symmetry point (C_1) and laser polarization vector plus a 1D slice of the potential on a line defined by the symmetry point (C_2) and the laser polarization vector. Correspondingly, when the 2D potential on a plane is reconstructed, we anticipate that it will represent the addition of the two parallel planes on which the symmetry points lie, that is, (001) and (002), shifted so that the symmetry centres coincide. This perspective is supported by the experimental results for the potential in Fig. 4c, which indeed represent the addition of the potentials on the two planes. For the CaF₂ experiments, the symmetry point of the crystal (marked as C) lies exclusively on the (002) plane as shown in Extended Data Fig. 5a. As a result, laser picoscopy probes only a single plane (Extended Data Fig. 5e).

Reconstructing the potential on a plane

The reconstruction of the potential on a plane requires information on the properties of the lattice. The MgF₂ crystal has a square lattice when seen from the c axis, the axis through which the laser impinges on the crystal in our experiments (Fig. 3a, b, insets). Although this information can be acquired from X-ray crystallography, laser picoscopy is independent from this information. Indeed, the lattice symmetries can be directly inferred by the angular dependence of the high-harmonic intensity yield as a function of the rotation of the crystal with respect to the c axis (Extended Data Fig. 4). This feature of high harmonics has been repeatedly demonstrated in previous studies^{7,8,13}. The 90° symmetry of these data directly suggests a square lattice.

A 2D potential slice $U(x, y)$ of a unit cell with a lattice constant d can be expanded in Fourier series as: $U(x, y) = \sum_{lm \in \mathbb{Z}} u_{lm} e^{i\frac{2\pi}{d}lx} e^{i\frac{2\pi}{d}my}$, where u_{lm} is the 2D Fourier coefficient of index l , and m and \mathbb{Z} denote integer numbers. To reconstruct a 2D picture of the potential, we need to identify u_{lm} . In our experiments, the Fourier coefficients of the 1D slice of the potential (\tilde{V}_k) along the characteristic crystal directions [100], [110] and [120] were first reconstructed. As described earlier, these Fourier coefficients are the projections of u_{lm} along the respective crystal directions. This fact is used to create a system of linear equations, which are in turn solved to obtain the amplitudes and phases of u_{lm} . Importantly, the symmetries of crystals give rise to numerous linear constraints, which reduce the number of unique unknowns of u_{lm} and simplify the problem dramatically. In this study, the system of equations was solved by a standard linear least square fitting method. The accuracy of the reconstruction depends on the number of unique 1D slices used to derive the 2D potential. To plot the 2D slice of the potential (Fig. 4c, Extended Data Fig. 5d), we kept all Fourier coefficients up to the seventh order implying a resolution of about 90 pm. Yet a more advanced implementation of this approach using several 1D potential slices acquired at different angles can restore the full resolution, which is currently available in the 1D measurements of the potentials as shown in the main text (about 26 pm).

Although in the current implementation of the technique the potentials in each slice are retrieved independently, two essential features of our approach allow their accurate combination to create 2D slices—and eventually 3D images—of the structure. The first is related to the fact that all reconstructed linear slices are centred around the same

Article

symmetry point of the crystal, or alternatively, the symmetry centre (expectation value of the position) of the crystal wavefunction within a unit cell. This implies that arbitrary phase shifts of the 1D potentials, before combining the data in a 2D picture, are not required. Second, although the 1D potential slices are reconstructed separately by the fitting of the normalized intensity harmonic yields, their relative amplitude can still be calibrated based on the variation of the harmonic yield in each direction. In the current implementation, the intensity yield of the lowest harmonic (third) was used to this end.

Reconstruction of valence potential and electron density of CaF₂ CaF₂ is best represented⁵⁶ by an expanded fcc lattice, composed of alternating layers of Ca and F atoms, as seen from the *c* axis (Extended Data Fig. 5a). A symmetry point (*C* in Extended Data Fig. 5a) of the crystal lies at the centre of the (002) (Ca plane). Therefore, we anticipate that in this crystal, laser picoscopy will be probing a single crystal plane—the Ca plane.

In the experiments, the pulses impinge on crystalline CaF₂ along the *c* axis (Extended Data Fig. 5a, orange curve). One-dimensional potential slices reconstructed by recording the intensity yield of harmonics versus the field strength (Extended Data Fig. 4) along the [110] and [100] axes are shown in Extended Data Fig. 5b, c, respectively. The derived 2D potential and electron density slices (for the plane (002)) are shown in Extended Data Fig. 5d, e, respectively as well as in Extended Data Fig. 6.

Beyond the anticipated dominance of Ca⁺² on plane (002), a notable contribution from F⁻ ions (Extended Data Fig. 5b, d, e) centred on the (004) plane is also observed. This can be attributed to the extended size of the ionic radius of fluorine compared with the distance between the (004) and (002) planes in CaF₂, as verified by DFT simulations (Extended Data Fig. 5f), and is suggestive of the high dynamic range provided by laser picoscopy. The radius, r^{\max} for Ca²⁺ as evaluated by the experimentally derived electron density is $r_{\text{Ca}^{2+}}^{\max} \approx 50$ pm, in agreement with the theoretical prediction⁴⁴ of about 54 pm.

Data availability

The datasets generated and/or analysed during this study are available from the corresponding authors on reasonable request.

Code availability

The analysis codes that support the findings of the study are available from the corresponding authors on reasonable request.

- Meng, S. & Kaxiras, E. Real-time, local basis-set implementation of time-dependent density functional theory for excited state dynamics simulations. *J. Chem. Phys.* **129**, 054110 (2008).
- Lian, C., Hu, S.-Q., Guan, M.-X. & Meng, S. Momentum-resolved TDDFT algorithm in atomic basis for real time tracking of electronic excitation. *J. Chem. Phys.* **149**, 154104 (2018).
- Runge, E. & Gross, E. K. U. Density-functional theory for time-dependent systems. *Phys. Rev. Lett.* **52**, 997–1000 (1984).
- Bertsch, G. F., Iwata, J.-I., Rubio, A. & Yabana, K. Real-space, real-time method for the dielectric function. *Phys. Rev. B* **62**, 7998–8002 (2000).
- Castro, A., Marques, M. A. L. & Rubio, A. Propagators for the time-dependent Kohn–Sham equations. *J. Chem. Phys.* **121**, 3425–3433 (2004).
- Perdew, J. P., Burke, K. & Ernzerhof, M. Generalized gradient approximation made simple. *Phys. Rev. Lett.* **77**, 3865–3868 (1996).
- Soler, J. M. et al. The SIESTA method for ab initio order-*N* materials simulation. *J. Phys. Condens. Matter* **14**, 2745–2779 (2002).
- Longhi, S., Horsley, S. A. R. & Della Valle, G. Scattering of accelerated wave packets. *Phys. Rev. A* **97**, 032122 (2018).
- Kak, A. C. & Slaney, M. *Principles of Computerized Tomographic Imaging* (Society for Industrial and Applied Mathematics, 2011).
- Hassan, M. T. et al. Optical attosecond pulses and tracking the nonlinear response of bound electrons. *Nature* **530**, 66–70 (2016).
- CaF₂ crystal structure: datasheet from PAULING FILE Multinaries Edition – 2012 *SpringerMaterials* https://materials.springer.com/isp/crystallographic/docs/sd_0378096 (2016).

Acknowledgements This work was supported by a European Research Council grant (Attoelectronics-258501), the Deutsche Forschungsgemeinschaft Cluster of Excellence, the Munich Centre for Advanced Photonics and the Max Planck Society.

Author contributions E.G. conceived and supervised the project. H.L., H.Y.K. and M.Z. performed the experiments and analysed the experimental data. H.Y.K. and H.L. performed the theoretical modelling and calculations. S.H. and S.M. conducted the DFT and TDDFT modelling. E.G., H.L. and H.Y.K. interpreted the experimental data and contributed to the preparation of the manuscript. These authors contributed equally: H. Lakhota, H. Y. Kim.

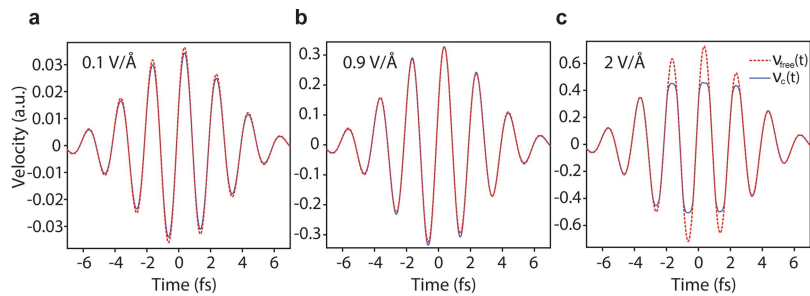
Competing interests The authors declare no competing interests.

Additional information

Correspondence and requests for materials should be addressed to E.G.

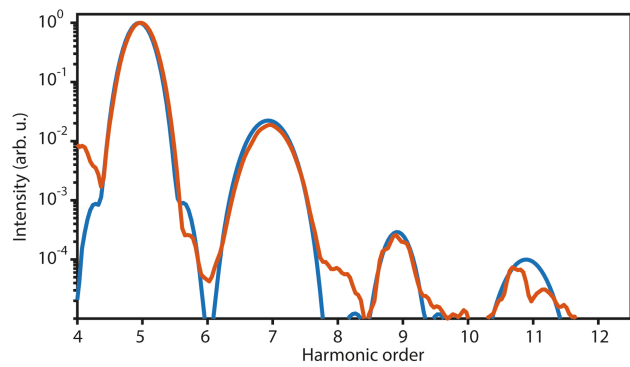
Peer review information *Nature* thanks Thomas Brabec, Michael Sentef, Andre Staudte and the other, anonymous, reviewer(s) for their contribution to the peer review of this work.

Reprints and permissions information is available at <http://www.nature.com/reprints>.

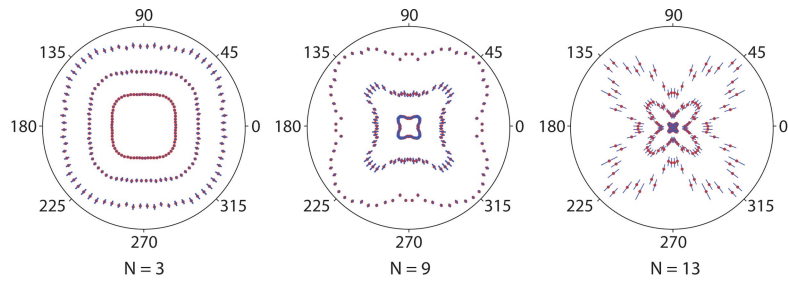


Extended Data Fig. 1 | Strong field-driven electron dynamics in MgF_2
 ($\hbar\omega_L = 2\text{eV}$). **a–c**, Comparison of crystal (v_c ; blue curves) and free (v_{free} ; red dashed curves) electron velocities along the [100] direction of an MgF_2 crystal

as calculated by TDDFT for laser field strengths F_0 of 0.1 V \AA^{-1} (**a**), 0.9 V \AA^{-1} (**b**) and 2.0 V \AA^{-1} , and carrier at an energy of $\hbar\omega_L = 2\text{eV}$.

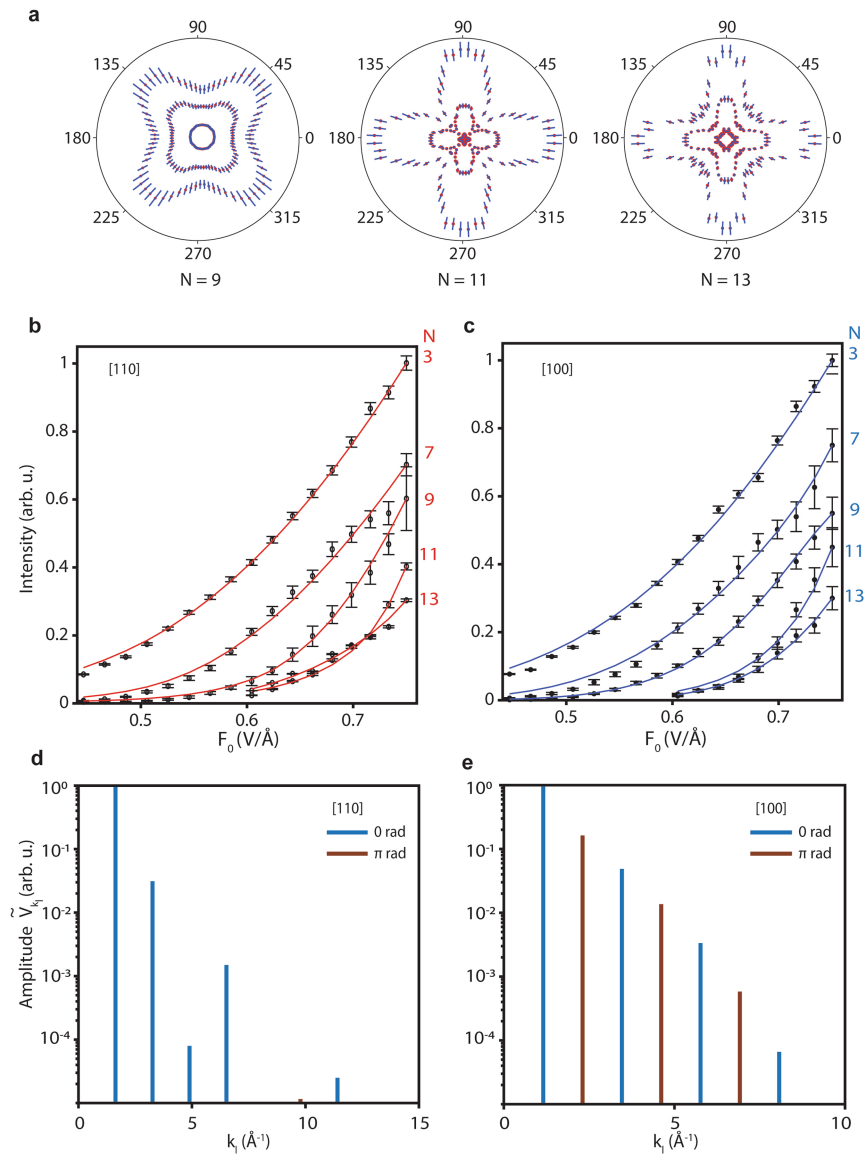
**Extended Data Fig. 2 | High-harmonic generation in MgF₂ (theory).**

High-harmonic spectra calculated by TDDFT simulations (red curve) and by use of the scattering model (blue curve) for laser parameters ($\hbar\omega_L = 2\text{eV}$ and $F_0 = 0.9\text{ V \AA}^{-1}$) and crystal orientation settings as quoted in Fig. 1d.



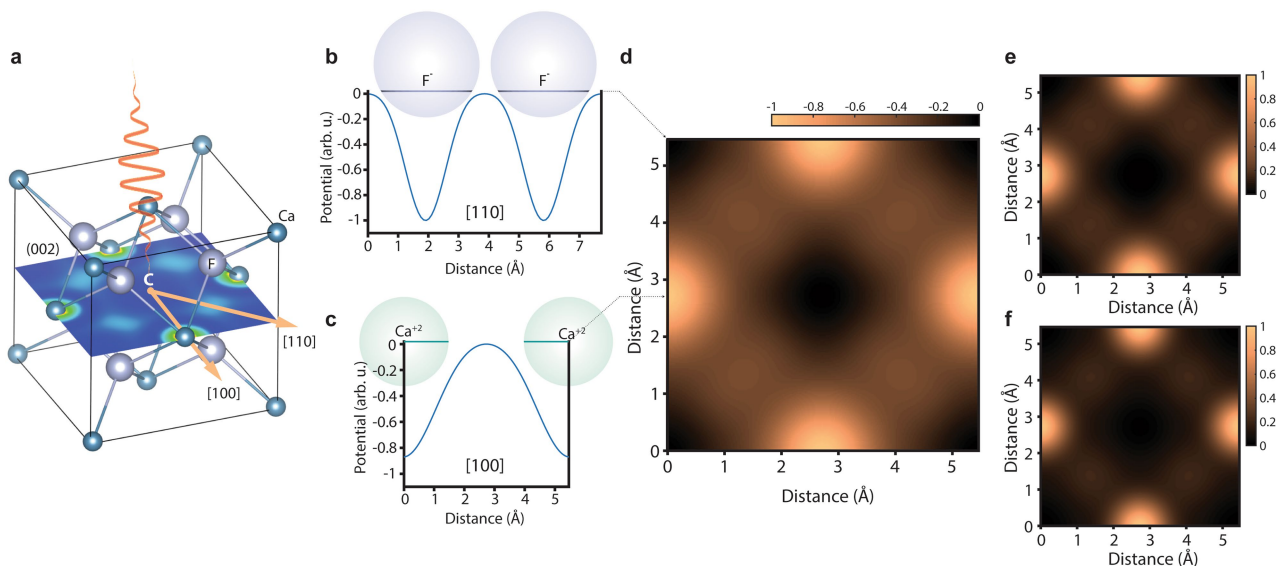
Extended Data Fig. 3 | Crystal orientation dependence of high-harmonic generation in MgF_2 . The intensity of the third, ninth and thirteenth harmonics measured as a function of the crystal angle at field strengths ($F_0 = 0.58, 0.65$ and 0.7 V \AA^{-1}) of the driving pulse. The rotation of the crystal is performed with respect to the c axis. The azimuthal angle represents the orientation of the

crystal with respect to the laser polarization and the radius represents the harmonic yield. The four-fold symmetry of the crystal suggests a square lattice. Error bars in the measured data indicate the standard deviation of the mean value from four measurements acquired under identical conditions.



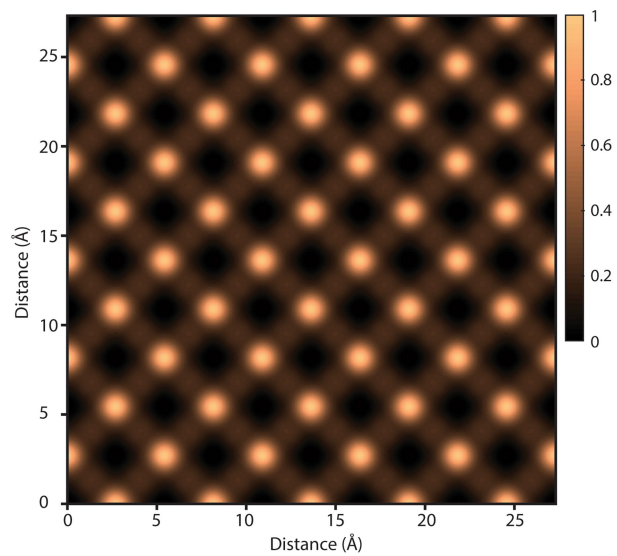
Extended Data Fig. 4 | Laser picoscopy in CaF₂. **a**, Intensity yields of representative harmonics ($N=9, 11$ and 13) in CaF₂ measured as a function of the crystal rotation angle with respect to the c axis and for three representative driving field strengths ($F_0 = 0.58, 0.65$ and 0.7 V \AA^{-1}). **b, c**, Intensity yields (black dots) of harmonics versus field strengths measured along the $[110]$ (**b**) and $[100]$ (**c**) axes of the crystal. The red and blue curves are the fitting of the

intensity yields according to equation (18) or equation (3). Error bars in **a-c** indicate the standard deviation of the mean value from three measurements acquired under identical conditions. **d, e**, Retrieved amplitudes \tilde{V}_{k_i} and their relative phases (0 rad in blue and $\pi \text{ rad}$ in red) along the $[110]$ (**d**) and $[100]$ (**e**) axes of the crystal.



Extended Data Fig. 5 | Reconstruction of the valence electron potential and density of CaF_2 . **a**, Crystal structure of CaF_2 . The laser pulse (orange curve) impinges on the crystal along the c axis. The potential is probed along lines determined by laser polarization vectors (orange arrows) and the symmetry point C . **b**, **c**, Reconstructed 1D slices of the valence potential (blue curves) when the laser polarization vector is aligned with the $[110]$ (**b**) and $[100]$ (**c**)

axes. Grey and cyan spheres represent F^- and Ca^{2+} , respectively, as aligned along the measurement line. **d**, Reconstructed 2D slice of the valence electron potential of CaF_2 on the (002) plane. Bright spots represent Ca^{2+} ions and the light broad spots represent F^- ions. **e**, Valence electron density evaluated from the data in **d**. **f**, DFT-calculated valence electron density of CaF_2 on the (002) plane.



Extended Data Fig. 6 | Electron density of CaF₂ extended over multiple unit cells. Bright dots correspond to Ca²⁺ ions centred on (002) plane while the light dots correspond to F⁻ ions centred on (004) plane but penetrating into the (002) plane.